

Understanding and Modeling the Effects of Task and Context on Drivers' Gaze Allocation

Iuliia Kotseruba and John K. Tsotsos

Abstract—Understanding what drivers look at is important for many applications, including driver training, monitoring, and assistance, as well as self-driving. Traditionally, factors affecting human visual attention have been divided into bottom-up (involuntary attraction to salient regions) and top-down (task- and context-driven). Although both play a role in drivers' gaze allocation, most of the existing modeling approaches apply techniques developed for bottom-up saliency and do not consider task and context influences explicitly. Likewise, common driving attention benchmarks lack relevant task and context annotations. Therefore, to enable analysis and modeling of these factors for drivers' gaze prediction, we propose the following: 1) address some shortcomings of the popular DR(eye)VE dataset and extend it with per-frame annotations for driving task and context; 2) benchmark a number of baseline and SOTA models for saliency and driver gaze prediction and analyze them w.r.t. the new annotations; and finally, 3) a novel model that modulates drivers' gaze prediction with explicit action and context information, and as a result significantly improves SOTA performance on DR(eye)VE overall (by 24% KLD and 89% NSS) and on a subset of action and safety-critical intersection scenarios (by 10–30% KLD). Extended annotations, code for model and evaluation will be made publicly available.

I. INTRODUCTION

Despite being commonplace, driving is inherently risky. Since lapsed or misplaced attention of drivers has been linked to increased odds of traffic accidents [1], much of the research on driver attention allocation has been safety-centered. In particular, a large body of research is dedicated to identifying and mitigating negative effects of engaging in non-driving related activities (e.g., using a cell phone) and investigating hazard anticipation [2].

In comparison, routine decision-making during driving is less studied. An important property of driving is that it is a visuomotor activity, i.e., motor actions of drivers are linked to vision, which provides most of the information [3]. However, drivers do not process the entire scene at once due to the limited field of view and varying acuity within it (foveation) [4]. Instead, they move their eyes sequentially to bring different elements of the scene into the fovea. Selection of the next location to look has been described in vision science as either *bottom-up* involuntary attraction to salient regions or *top-down* task-driven sampling of areas relevant to current or future action [5], [6]. Both play a role during driving; bottom-up cues help react to signals and signs (salient by design) [7] and potential hazards [8], [9], and top-down strategies are important for safely steering the vehicle along the planned

route. For example, at intersections, drivers display different gaze patterns depending on maneuver, presence and status of traffic signals, road layout, and actions of other road users [10], [11], [12], [13]. Even though there is significant evidence for top-down effects on directing drivers' gaze, most of the existing models do not explicitly include them. Furthermore, driving datasets with attention-related data do not contain labels relevant to the task and context, thus making training models and evaluating their performance with respect to these factors difficult. To this end, here, we propose an extension of the popular DR(eye)VE dataset [14], a benchmark focusing on task- and context-relevant features, a new model combining visual and task-relevant data for predicting drivers' gaze, and experiments investigating the effects of various task and context representations.

II. RELATED WORKS

Visual attention. Research on estimating and predicting driver's gaze is rooted in the field of vision science studying bottom-up (data-driven) and top-down (task-driven) influences on attention [5], [6]. The majority of the models proposed to date perform bottom-up saliency prediction in static images and video sequences by identifying properties of rare or out-of-context visual features that attract gaze [15], [16]. Top-down attention, on the other hand, is relatively less studied and is typically investigated within the paradigm of visual search involved in many common activities [17]. In the early works [18], [19], characteristics of the search target (e.g., color) were used to adjust weights of bottom-up features in the output. Modern deep learning models continue to explore modulation techniques during feedforward [20], [21], [22] and backward passes [23], [24], [25] for a range of applications beyond visual search, e.g., object detection, segmentation, and visuo-linguistic tasks.

Driver gaze prediction. Models for predicting drivers' gaze can likewise be subdivided by the types of attentional mechanisms they model and stimuli they use. The majority of deep learning methods achieve promising results on drivers' gaze prediction benchmarks by learning associations between images of the scene and human saliency maps in a bottom-up fashion. Image-based models use CNNs pretrained on an image classification task to encode visual information and then apply convolution and upsampling layers to generate gaze maps [26], [27]. Video-based models aim to extract spatio-temporal patterns from stacks of frames; DR(eye)VENet [14], SCAFFNet [28], and MAAD [29] use a 3D CNN pretrained on action classification task as an encoder, whereas BDD-ANet [30] and ADA [31] extract

Both authors are with the EECS Department of Computer Science and Electrical Engineering, York University, Canada. Email: {yulia84, tsotsos}@yorku.ca

features from each frame via a pretrained CNN and then feed them into a ConvLSTM. Many models use features in addition to visual input, such as optical flow [26], [14], [29], segmentation maps [14], [32], [28], and depth [32].

Top-down influences are often modeled by blending bottom-up saliency outputs with driving-task-related features, such as vanishing point [33], [34], [35], where drivers often maintain gaze [36], drivers’ actions derived from vehicle telemetry [37], [38], or gaze location priors associated with certain actions [39]. A recent HammerDrive model [40] recognizes maneuvers, e.g., lane changes, from vehicle data and uses this information to assign weights to bottom-up saliency predictors trained on each task. MEDIRL [41], learns attention policy via inverse reinforcement learning, where agent state is represented by the vehicle telemetry, as well as local and global context extracted from visual input.

Driving datasets. Publicly available large-scale datasets comprised of driving footage and gaze information greatly boosted research on drivers’ gaze prediction. The first such dataset, 3DSS [37], was recorded in a video game environment. More recent ones are captured either on the road with drivers wearing head-mounted eye trackers (e.g., DR(eye)VE [14] and LBW [42]) or use pre-recorded naturalistic footage that human subjects can view in the lab (e.g., BDD-A [30] and DADA-2000 [43]). However, task-relevant information that can be effectively used for training and evaluation is usually not available or incomplete. For example, only parts of DR(eye)VE dataset with unusual gaze patterns are annotated as “acting” without specification of the action being performed by the driver. Similarly, in BDD-A, ground truth deviating from the mean is associated with drivers’ actions or sudden events without explicit class labels. The authors of [39] and [41] evaluate models on different types of scenarios from DR(eye)VE and BDD-A dataset, but do not make the annotations available.

Contributions: 1) we address the lack of consistent task-relevant annotations by manually labeling drivers’ actions and relevant context elements in the popular DR(eye)VE benchmark and remedy some shortcomings of the existing ground truth; 2) using the new annotations, we create a benchmark to analyze relative performance of the state-of-the-art (SOTA) models on the entire dataset and with respect to task and context factors; and 3) propose a model that demonstrates advantages of task-relevant information for modulating bottom-up driver gaze prediction.

III. EXTENDING DR(EYE)VE

We chose DR(eye)VE [14] since it is recorded in real road conditions *and* provides all raw data, including eye tracker output and ego-vehicle telemetry. This combination of ecological validity and rich data makes it the most suitable starting point among datasets listed in the previous section.

A. Original ground truth

DR(eye)VE consists of 6 hours (0.55M frames) of driving footage and gaze data recorded on-road in an actual vehicle. Eight participating drivers wore eye-tracking glasses (ETG)



Fig. 1: Example of misalignment by 9 frames. The car in the driver’s view (ETG) is to the left of the ego-vehicle but is to the right in the rooftop camera view (GAR_{orig}). Our recomputed GAR_{new} shows a correct alignment.

which allowed free head movement. Due to the insufficient quality of the eye tracker world-facing camera, its limited view, and drivers’ head movements, an additional wide-angle Garmin camera (GAR) was installed on top of the vehicle’s roof. Ground truth saliency maps were created following a two-stage procedure: 1) drivers’ gaze coordinates were mapped from driver’s view (ETG) to the rooftop camera view (GAR) via a geometric transformation; 2) since each recording was associated with a single driver’s gaze, only a handful of data points were recorded per frame. Thus, to reduce sparsity and individual drivers’ biases, data points were aggregated over a sliding window of 25 frames (1s).

B. New ground truth

As we examined the raw eye-tracker output and ground truth data in DR(eye)VE, several irregularities were identified: 1) temporal misalignment of the world-view eye-tracking glasses camera (ETG) and rooftop camera (GAR) video streams; 2) incorrect inclusion of saccades and blinks in the ground truth; 3) incorrect inclusion of drivers’ gaze towards the vehicle interior and outside the rooftop camera view; 4) noisy homography transformations for mapping gaze from ETG to GAR and aggregating gaze across GAR frames; and 5) artifacts caused by the Gaussian response function used to compute the original ground truth. Below, we discuss how we addressed each of these shortcomings (see for more details).

Video re-alignment. Due to different frame rates of the cameras, each ETG and GAR video contains 9000 and 7500 frames, respectively. The original mapping between ETG and GAR frames is consistent with linear interpolation. However, upon closer inspection, we found that videos were not aligned temporally (Figure 1); often, the GAR camera continued recording up to 15–20 frames (0.5–0.8s) after the ETG camera stopped. In some videos, the cameras also did not start recording at the same time. Since videos did not contain timestamps, we manually aligned them using events visible in both camera views, such as windshield viper movement, traffic light changes, etc. Most videos were misaligned by 7 ± 5 frames on average, 40% of the videos by up to 15 frames (0.5s) and 10% by over 25 frames (1s).

Removal of saccades, blinks, and in-vehicle fixations, remedying out-of-bounds fixations. Eye-tracking glasses used for data collection provide labels for fixations, saccades, blinks, and recording errors. The distribution of these events is shown in Figure 2. Although it is common to filter out saccades and blinks from ground truth, saliency maps provided with DR(eye)VE contain both. Since during blinks

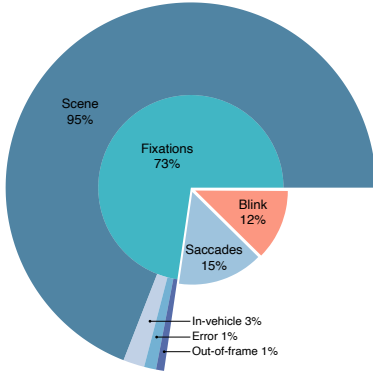


Fig. 2: Composition of eye-tracking data in DR(eye)VE. Inner circle: % of data points labeled as fixations, blinks, and saccades. Outer circle: spatial distribution of fixations.



Fig. 3: Irregularities in the original ground truth and proposed corrections. ETG and GAR show driver’s and rooftop camera views, respectively, with fixations (red circles) at time t . Original (GT_{orig}) and new (GT_{new}) ground truth aggregate fixations over frames $t \pm 12$ (1s). Top row: The “trail” of points in GT_{orig} corresponds to a saccade towards the speedometer and is absent in GT_{new} after removal of saccades and in-vehicle fixations. Bottom row: Incorrect mapping of driver’s gaze outside the GAR view results in a random pattern in GT_{orig} . In GT_{new} , such out-of-frame fixations are pushed towards the edge of the frame to preserve the direction and elevation of the driver’s gaze.

and saccades vision is largely suppressed [44], inclusion of such data effectively biases the dataset by implying that the driver perceived something at those locations. Saccades also produce “trails” in the ground truth maps due to temporal aggregation (see Figure 3, top row). Therefore, all non-fixations are excluded from the new ground truth.

In DR(eye)VE, 95% of fixations fall on the windshield and only a small fraction is directed at the vehicle interior or towards the side windows (Figure 2):

- *In-vehicle gaze.* Nearly 3% of all fixations are directed towards the speedometer, mirrors, and passengers in the vehicle. When projected onto the scene, these gaze points will incorrectly reflect what the driver was looking at. We manually annotated fixations towards vehicle interior and removed those irrelevant to the driving scene (e.g., speedometer, passengers) from the ground truth.
- *Errors.* Fixations that were far out of bounds in the ETG camera view (1% of the total) were removed as they could not be reliably mapped to GAR view.
- *Gaze outside the camera viewpoint.* When the driver turns their head, e.g., to look through side windows or over the shoulder, their gaze often falls outside the rooftop camera

TABLE I: Counts, durations (in frames), and % of frames containing lateral and longitudinal actions, and intersections

	Actions/context	Count	Mean	Std	% frames
Lateral actions	Drive straight	1497	335.20	643.15	93.0
	Turn right	97	171.98	120.51	1.8
	Turn left	69	184.81	128.58	1.6
	Lane change right	35	458.03	1072.52	1.7
	Lane change left	26	219.73	356.80	1.7
Long. actions	Maintain	688	503.64	933.41	62.4
	Accelerate	482	192.47	112.24	13.7
	Decelerate	480	157.91	75.79	16.7
	Stopped	88	453.75	431.94	7.2
Inters. type	Roundabout	58	63.83	19.55	0.67
	Merge	159	33.28	20.18	0.95
	Signalized	106	48.74	85.94	0.93
	Unsignalized	541	47.74	47.42	3.65

(GAR) view (see Figure 3, bottom row). In the original dataset, these fixations were erroneously mapped onto the scene (causing random patterns in ground truth) or manually removed (resulting in blank ground truth) but not marked in annotations. We manually labeled all such fixations. Since they are present in virtually all safety-critical scenarios (e.g., intersections), in the new ground truth, we push out-of-frame fixations towards the edge of the image to preserve the direction and elevation of driver’s gaze.

Re-computing and manual correction of projected fixations. Video re-alignment changed $\approx 90\%$ of the correspondences between ETG and GAR frames, therefore we could no longer use the pre-computed homographies supplied with the dataset to map gaze from ETG to GAR view. We used the VLFeat library [45] with the same parameters and thresholds as in the original implementation to compute homography transformations for the new alignment, inspected the results, and manually corrected all outliers.

Data re-aggregation. Although use of homography is justified in case of ETG-GAR transformation, it is less so for aggregating GAR frames across a 1s temporal window. Since the main purpose of this transformation is to compensate for motion in the scene, we instead apply a technique from [46] that relies on optical flow. We use RAFT [47] to compute optical flow and then use its magnitude and direction to trace locations of fixations from frames $t - 12, \dots, t - 1$ and $t + 1, \dots, t + 12$ to the key frame t .

Generating heatmaps. The original ground truth is computed as a max over Gaussian response function for each data point in the temporal window. Here, we set the fixated locations to 1 and apply an isotropic Gaussian filter with the size of 40 px, roughly equal to human fovea radius following [48], [49], [50], [51]. The final result is shown in Figure 3.

C. Extended annotations

To analyze the effects of tasks and context on gaze, we extended the annotations. Here, *task* is a series of maneuvers (actions) that the drivers perform on the route to their destination. *Context* is defined as the intersections along the route and drivers’ priority during the maneuver, i.e., whether they have a right-of-way or must yield to other road users.

Task annotations. Drivers’ actions were divided into lateral and longitudinal and annotated per-frame. For lateral actions, we identified and manually labeled *left/right turns* and *lane*

TABLE II: Results on original and new DR(eye)VE ground truth, and action and context subsets of the new ground truth. \uparrow and \downarrow indicate that larger and smaller values are better. Best and second-best values are shown as **bold** and underlined.

		DR(eye)VE _{orig}				DR(eye)VE _{new}				Actions (KLD↓)					Roundabout		Highway ramp		Signalized		Unsignalized	
	Model	KLD↓	CC↑	NSS↑	SIM↑	KLD↓	CC↑	NSS↑	SIM↑	Stop	None	Lat	Lon	Lat+Lon	RoW	Yield	RoW	Yield	RoW	Yield	RoW	Yield
Image	CDNN†	5.33	0.36	1.75	0.24	4.22	0.44	1.51	0.32	7.82	3.11	7.02	5.26	9.23	6.66	10.06	1.66	8.17	5.39	5.99	5.12	13.81
	CDNN**	2.69	0.54	2.45	0.35	2.00	0.67	2.03	0.54	5.77	1.38	3.39	2.09	4.09	2.66	4.72	1.23	7.29	2.43	3.23	1.76	6.17
	DeepGaze II	3.10	0.25	1.25	0.13	2.52	0.30	1.13	0.16	3.04	2.37	3.24	2.55	3.50	2.85	3.22	2.35	3.87	2.73	3.09	2.73	4.81
	UNISAL	2.78	0.34	1.82	0.16	2.40	0.40	1.73	0.21	3.02	2.13	3.97	2.56	4.63	2.75	4.34	2.06	7.87	2.57	3.68	2.57	8.73
Video	UNISAL	3.10	0.45	2.26	0.30	2.16	0.54	2.05	0.39	4.28	1.63	4.80	2.49	6.82	2.35	7.48	1.33	7.43	2.81	4.91	2.86	11.69
	BDD-ANet†	3.15	0.47	2.08	0.32	2.07	0.57	1.72	0.41	3.35	1.66	3.62	2.28	4.45	2.18	4.89	1.41	7.96	2.31	4.39	2.13	6.96
	BDD-ANet**	2.55	0.51	2.31	0.35	1.61	0.64	2.05	0.48	3.20	1.21	2.70	1.77	3.29	2.56	3.96	1.04	5.96	1.91	2.42	1.69	4.28
	DreyeVENet**	2.63	0.54	2.43	0.39	2.13	0.67	2.01	0.56	3.38	1.56	4.17	2.68	4.90	3.15	7.59	1.37	8.02	2.42	4.48	2.30	7.68
	ADA†	2.33	0.56	2.41	0.39	1.33	0.68	2.00	0.51	2.41	1.08	2.65	1.43	2.85	1.78	2.72	0.91	6.77	1.43	2.09	1.45	4.07
	ViNet	1.97	0.48	2.42	0.30	1.37	0.59	2.21	0.40	2.29	1.13	2.04	1.51	2.64	1.87	3.05	1.00	2.57	1.62	2.17	1.50	3.95
	ViNet*	1.81	0.54	2.34	0.34	1.21	0.66	1.99	0.48	2.43	0.96	1.76	1.33	2.13	1.78	2.69	0.89	1.97	1.46	2.11	1.30	2.58

* — model is trained on data; \dagger — model for drivers' gaze prediction. Stop — ego-vehicle is stopped, Lat — lateral actions only, Lon — longitudinal only, None — no action, RoW — ego-vehicle has right-of-way. Green and red colors indicate the best and worst values, respectively, to highlight challenging scenarios. We compute KLD using code in [52] since it is more numerically stable than implementation in [14] used to produce results reported in other literature. Note that while the absolute KLD values are different, the relative ranking of the models is preserved. See Section C.1 for additional details on KLD and Table VII for results for other metrics.

changes, as well as *U-turns*. The rest were labeled as *driving straight*. To produce longitudinal action labels, we first interpolated and smoothed vehicle speed with an average filter, and computed acceleration from these values. *Stopped* labels were assigned to segments where speed did not exceed 1 km/h, threshold for *acceleration* and *deceleration* labels was set to ± 0.4 m/s². Table I shows statistics of the action labels in the dataset. Less than 7% of all frames contain lateral actions, whereas longitudinal actions take place in 27% of the frames, and only 4% of the frames contain both longitudinal and lateral action.

Context annotations. Context annotations include *intersection locations* and *types*, as well as drivers' *priority* while passing the intersection. The following intersection types are annotated: *roundabouts*, *highway on-ramps*, *signalized* (controlled by traffic lights), and *unsignalized* (sign-controlled or uncontrolled) intersections. For intersections, where the driver yielded to opposing traffic, we count frames from the first time that the driver fixated on the intersecting road. When the driver has a right-of-way, we consider preceding 25 frames, due to the approx. 1s gaze-action delay [53]. Table I shows the counts and duration of video segments that contain intersections, accounting for $\approx 7\%$ of all frames. Action and context categories are balanced across training and test sets.

IV. BENCHMARK RESULTS

In this section, we evaluate a number of models including SOTA generic bottom-up saliency algorithms (DeepGaze II [54], UNISAL [55], ViNet [56]) and drivers' gaze prediction algorithms (CDNN [33], DreyeVENet [14], BDD-ANet [30], and ADA [31]) that operate on image and video data (UNISAL works on both). We report the evaluation results using common saliency metrics: Normalized Scanpath Saliency (NSS), histogram similarity (SIM), Pearson's correlation coefficient (CC), and Kullback–Leibler divergence (KLD) [57]. We train and evaluate the models on original and new ground truth. Blank ground truth frames and frames

that contain U-turns are excluded from evaluation¹.

Overall performance. Results presented in Table II lead to two observations. First, performance of all models improves significantly on all metrics when trained or evaluated on the new ground truth data, which can be attributed mainly to the removal of a large number of blinks and saccades as well as to the reduction of artifacts introduced by the original fixation aggregation procedure (see Figure 3). Second, generic saliency models (particularly image-based ones) do not generalize well to driving data, but when trained, can perform on par or better than driving-specific gaze prediction models. For example, ViNet outperforms driving-specific models on some metrics despite not using any additional information (e.g., semantic segmentation and optical flow as in DreyeVENet) or weighted sampling (as in BDD-ANet).

Effects of task. Using the new task and context annotations, we analyze performance of the models with respect to various aspects of task and context, namely, driver's actions, intersections types, and ego-vehicle priority when passing through them. In Table II, the results are aggregated over different types of actions, as well as times when the ego-vehicle is not moving or is maintaining lane/speed. Naturally, predicting *stop* sequences is more challenging, since drivers' gaze tends to wander around the scene. In *no action* sequences, drivers predominantly look at the vanishing point or lead vehicle, thus all models perform well across all metrics. Longitudinal actions pose less challenge than lateral actions since they still require the driver to primarily attend to the objects located in front, such as the lead vehicle and traffic signals or signs. Lateral actions often involve checking mirrors and scanning across the scene, therefore are more difficult to predict. Finally, both lateral and longitudinal actions are needed when passing through intersections, interacting with other road users, or both. Since

¹Blank gt maps result from gaze data missing due to blinks/saccades/errors and may cause issues with some metrics. U-turns are removed because there are only 14 instances, all in dead ends with no traffic, and most gaze information is lost since the driver looks at the mirrors or over the shoulder.

such scenarios are the least represented in the training set and contain the most complex gaze patterns, performance of all models on this subset is reduced across all metrics.

Effects of context. Table II shows results aggregated by four intersection types and two priority options. Here, we observe that sequences where ego-vehicle must yield to other road participants leads to a dramatic drop in performance for all models. Yielding scenarios are generally more complex since the driver must check different areas of the road (e.g., look to the left and right for incoming traffic), often in advance, and irrespective of presence of other road users. Given the enormous variability of possible scenarios in each context and a small number of samples in the training data, the bottom-up learning strategy used in all tested models struggles to capture such gaze patterns. However, not all intersection types are equally challenging. Roundabouts and unsignalized intersections are more difficult since they always require the driver to check the surroundings and often to negotiate with other road users. Whereas when passing signalized intersections or merging on a highway, gaze patterns are simpler since drivers tend to observe the same areas, e.g., looking towards the lane immediately to the left when entering highway on-ramp or checking the traffic approaching from the opposite direction when making an unprotected left turn².

V. SCOUT: TASK- AND CONTEXT-MODULATED ATTENTION

Next, we explore integration of the new task and context annotations for modulating gaze prediction. The problem is formulated as follows: given a set of video frames and a set of labels representing task and context information, predict a human gaze map for the last frame of the set.

A. Model architecture

The architecture of SCOUT comprises three modules: an encoder for visual and task/context features, modulation blocks, and a decoder (as shown in Figure 4).

Encoder. To encode video data, we use Video Swin Transformer (VST) [58] as a backbone for spatio-temporal feature extraction. Compared to C3D [59] and S3D [60] backbones used in other saliency models [14], [56], VST is lightweight and performs better on action recognition benchmarks, which is useful for transfer learning. VST takes a set of 16 frames as input and outputs features from each of its four blocks.

Task and context input consists of per-sample text labels and per-frame numeric values (indicated as l_1, \dots, l_n and n_1, \dots, n_m in Figure 4), representing *global context* (weather, time of day, and location labels provided with DR(eye)VE), *local context* (next lateral action label, distance to next intersection (m) derived from GPS, and priority label), and *current action* (speed in km/h, acceleration in m/s^2 , and lateral action label). See also Section B. We use a linear embedding layer to encode text labels and downsample

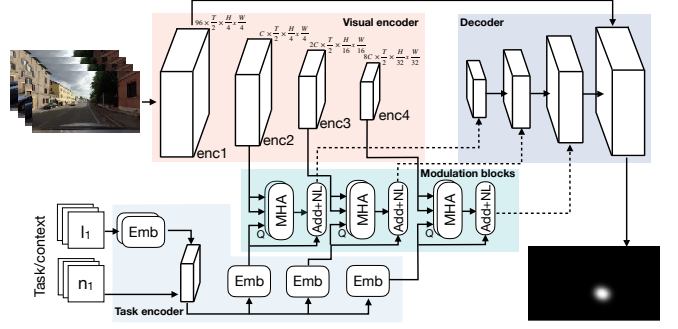


Fig. 4: Architecture of SCOUT model: two encoders for visual and task/context data, multi-head attention (MHA) modulation blocks, and a decoder. Text labels l_1, l_2, \dots, l_n and numeric features n_1, n_2, \dots, n_m represent task and context information. Arrows from the modulation blocks into the decoder are shown as dashed for readability.

the numeric values along the temporal dimension to match the temporal dimension of VST outputs. We then stack the encoded features, apply an affine transformation to match the feature dimension C of the corresponding encoder block and replicate the features across that block's spatial dimensions.

Modulation blocks. We modulate spatio-temporal visual features with task and context information via cross-attention using multi-head attention (MHA) [61], following the success of this technique for modulating attention with visual [22] and multi-modal features [62]. Encoded task features are passed to the MHA as queries, and visual features are used as keys and values. We then add the initial task features to the MHA output and apply layer normalization (LN).

Decoder. The decoder gradually fuses information from encoder and modulation blocks, while increasing their spatial dimension and reducing the channel and temporal dimensions. Each of the decoder blocks consists of one upsampling layer, ReLU layer, and 3D convolution layer. The output of each encoder or modulation block is first upsampled and concatenated with the preceding block. The result is fed through ReLU layer and then into the 3D convolutional layer.

B. Implementation details

We use the Swin-S Video Swin Transformer model [58] pre-trained on the Kinetics-400 dataset [63] as encoder backbone and continue to update its weights during training. The input to the network is a set of 16 consecutive frames ($\approx 0.5s$ observation) resized to $224 \times 224 \times 3$. MHA blocks used for modulating visual data with task and context information each have 2 heads and embedding sizes set to match the C dimension of the corresponding encoder blocks. We use the first 35 videos from DR(eye)VE dataset for training, videos 35–37 for validation, and the remaining videos for testing. Training samples are generated by splitting the videos into 16-frame segments with 8 frame overlap. Sequences with blank ground truth and U-turns are excluded from training, validation, and testing, as explained earlier in Section IV. The model is trained on a single NVIDIA Titan 1080Ti GPU for 20 epochs with the KLD loss, Adam optimizer [64], early

²Evaluation on other metrics (CC, NSS, and SIM) on actions and context subsets reveals similar patterns as KLD shown. Due to limited space, these results will be released with the code for the paper.

TABLE III: Performance of SCOUT model without task, with weighting, and with task and context information. \uparrow and \downarrow indicate that larger and smaller values are better. Best and second-best values are shown as **bold** and underlined, respectively.

		DR(eye)VE _{new}				Actions (KLD \downarrow)					Context (KLD \downarrow)							
Model		KLD \downarrow	CC \uparrow	NSS \uparrow	SIM \uparrow	Stop	None	Lat	Lon	Lat+Lon	Roundabout		Highway ramp		Signalized		Unsignalized	
ADA \dagger		1.33	0.68	2.00	0.51	2.41	1.08	2.65	1.43	2.85	RoW	Yield	RoW	Yield	RoW	Yield	RoW	Yield
ViNet \dagger		1.21	<u>0.66</u>	1.99	0.48	2.43	0.96	1.76	1.33	2.13	1.78	2.69	0.89	<u>1.97</u>	1.46	2.11	1.30	2.58
SCOUT	w/o task	1.08	0.63	3.89	0.52	2.42	0.81	1.61	1.25	2.02	1.26	2.89	0.74	2.24	1.15	2.46	1.10	3.11
	w/o task + weighted loss	1.01	0.65	4.04	0.51	2.05	0.77	1.82	1.15	1.55	1.41	2.60	0.72	2.26	1.09	1.88	1.02	2.74
	w/o task + weighted sampling	1.01	0.65	4.02	0.52	2.24	0.76	1.75	1.14	1.55	1.51	2.61	0.66	2.12	1.16	1.77	1.01	2.62
	w/ task CA[3]	0.97	<u>0.66</u>	4.06	0.52	2.05	<u>0.73</u>	1.53	1.11	1.80	<u>1.29</u>	2.43	<u>0.64</u>	2.29	1.08	1.90	1.04	2.42
	w/ task GC+LC+CA [2, 3, 4]	0.95	<u>0.66</u>	4.09	<u>0.54</u>	1.94	<u>0.73</u>	<u>1.44</u>	<u>1.06</u>	1.60	1.58	<u>1.99</u>	<u>0.64</u>	2.21	1.03	2.12	<u>0.93</u>	<u>2.13</u>
	w/ task GC+LC+CA [3]	<u>0.94</u>	0.67	<u>4.13</u>	<u>0.54</u>	2.09	0.70	<u>1.44</u>	1.05	<u>1.53</u>	1.52	1.90	0.57	2.07	<u>1.01</u>	1.50	0.97	2.14
w/ task LC [2]		0.92	0.67	4.17	0.55	<u>2.03</u>	0.70	1.39	1.05	1.48	1.43	2.03	0.67	1.95	0.99	<u>1.60</u>	0.89	2.09

* — model is trained on the data; \dagger — model for drivers' gaze prediction. Task/context input: GC — global context, LC — local context, CA — current action. [] — numbers in square brackets are indices of encoder blocks (shown in Figure 4) modulated with task/context information. Results for additional metrics are shown in Table VIII.

stopping based on validation loss, a constant learning rate of $1e-4$, and a batch size of 4.

C. Results

Table III shows the evaluation results of the SCOUT model variants with and without task information on the entire DR(eye)VE dataset, as well as subsets of it corresponding to different types of actions and context as defined in Section III-C. ADA and ViNet, models with the strongest results on action/context in Section IV, are shown for reference.

Performance without task information. We begin by establishing the baseline performance of the proposed model without task information. SCOUT without task improves SOTA results on all metrics, except CC, by a large margin. In particular, it improves NSS (highly sensitive to false positives) by 76% and KLD (that penalizes false negatives) by 11% overall, and achieves better results on some actions and context subsets (by up to 5–30% KLD). This can be partially attributed to more meaningful spatio-temporal features extracted by the VST compared to other backbones.

We also investigate other techniques, such as weighted sampling (as in [30]) and weighted loss. For both, we compute per-sample weight as a mean KLD score between sample ground truth and average saliency map for the video from which the sample is extracted. It has been hypothesized that samples that deviate from average contain important events [30], [14], [41] and therefore choosing such samples more often during training or using the weight to penalize errors may be beneficial. Although both techniques lead to an additional overall improvement of 6% KLD and 4% NSS, high sample weights are not always correlated with drivers' actions and may instead amplify noise, leading to only minor improvements on some action and context subsets.

Effects of task and context input. Lastly, we experiment with task and context input to SCOUT: we vary the types of task/context features and whether they are incorporated into a single encoder block or several. The results in Table III indicate that any additional information is beneficial overall (89% better on NSS and 24% on KLD compared to SOTA, and 2–8% across all metrics w.r.t. SCOUT w/o task) and especially for action and context subsets (10–30% KLD over SOTA and SCOUT w/o task). The overall best performance is reached when task/context features are added to the second

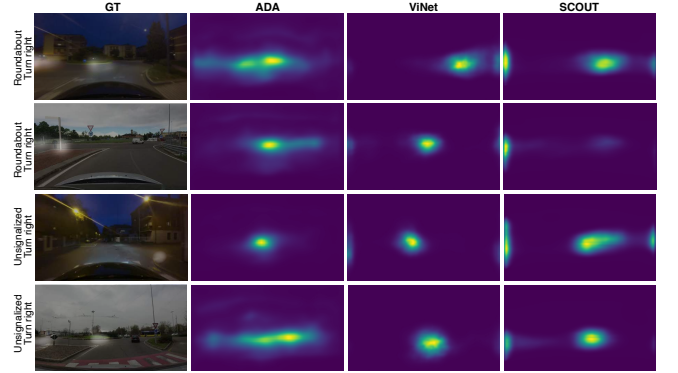


Fig. 5: Examples of yielding scenarios at different intersections types while performing a turn. The ground truth (in white) is overlaid on top of the images in the first column.

and third encoder blocks, presumably because they contain richer semantic information than earlier blocks and can take advantage of such representation. Significant performance gains (20–25% KLD) are also achieved on the yielding scenarios at roundabouts and unsignalized intersections. This is demonstrated in Figure 5 rows 1, 2, and 4. Note that SCOUT accurately highlights the left side of the upcoming intersection where conflict vehicles may appear, whereas other models remain centered. At the same time, some right-of-way subsets (roundabout and highway) see a slight decline in performance, caused by the model learning to always check the edges of the road near the intersections (see row 3 in Figure 5) even if the ego-vehicle has the right-of-way.

VI. CONCLUSION

In this paper, we discussed analyzing and modeling effects of task and context on drivers' gaze prediction. First, we extended the existing DR(eye)VE dataset with task- and context-related annotations and used them to demonstrate that most models do not capture gaze patterns typical for underrepresented and safety-critical scenarios, such as turning and yielding at intersections. We then showed via the proposed model that modulation with explicit task and context information is more effective than bottom-up learning or sampling strategies used in prior works. One limitation of the proposed model is reliance on manually annotated task labels due to noisy and incomplete vehicle information provided

with the DR(eye)VE dataset (e.g., inaccurate GPS and no yaw output useful for detecting lateral actions). In future work, we will explore methods for automatic extraction of these and other features representing context (e.g., other road users) and other methods for modulating gaze prediction.

Acknowledgement. This work was supported by the Natural Sciences and Engineering Research Council of Canada (NSERC), the Air Force Office for Scientific Research (USA), and the Canada Research Chairs Program through grants to JKT.

REFERENCES

- [1] J. K. Caird, K. A. Johnston, C. R. Willness, and M. Asbridge, "The use of meta-analysis or research synthesis to combine driving simulation or naturalistic study results on driver distraction," *Journal of Safety Research*, vol. 49, pp. 91–96, 2014.
- [2] I. Kotseruba and J. K. Tsotsos, "Behavioral research and practical models of drivers' attention," *arXiv:2104.05677*, 2021.
- [3] M. Sivak, "The information that drivers use: is it indeed 90% visual?," *Perception*, vol. 25, no. 9, pp. 1081–1089, 1996.
- [4] G. Osterberg, "Topography of the layer of the rods and cones in the human retina," *Acta Ophthalmologica*, vol. 13, no. 6, pp. 1–102, 1935.
- [5] J. K. Tsotsos, *A computational perspective on visual attention*. MIT Press, 2011.
- [6] K. Nobre and S. Kastner, *The Oxford Handbook of Attention*. Oxford University Press, 2014.
- [7] J. S. McCarley, K. S. Steelman, and W. J. Horrey, "The View from the Driver's Seat: What Good Is Saliency?," *Applied Cognitive Psychology*, vol. 28, no. 1, pp. 47–54, 2014.
- [8] P. R. Chapman and G. Underwood, "Visual search of driving situations: Danger and experience," *Perception*, vol. 27, no. 8, pp. 951–964, 1998.
- [9] G. Underwood, P. Chapman, Z. Berger, and D. Crundall, "Driving experience, attentional focusing, and the recall of recently inspected events," *Transportation Research Part F: Traffic Psychology and Behaviour*, vol. 6, no. 4, pp. 289–304, 2003.
- [10] J. Werneke and M. Vollrath, "What does the driver look at? The influence of intersection characteristics on attention allocation and driving behavior," *Accident Analysis & Prevention*, vol. 45, pp. 610–619, 2012.
- [11] J. Werneke and M. Vollrath, "How do environmental characteristics at intersections change in their relevance for drivers before entering an intersection: Analysis of drivers' gaze and driving behavior in a driving simulator study," *Cognition, Technology & Work*, vol. 16, no. 2, pp. 157–169, 2014.
- [12] S. Lemonnier, R. Brémond, and T. Baccino, "Gaze behavior when approaching an intersection: Dwell time distribution and comparison with a quantitative prediction," *Transportation Research Part F: Traffic Psychology and Behaviour*, vol. 35, pp. 60–74, 2015.
- [13] G. Li, Y. Wang, F. Zhu, X. Sui, N. Wang, X. Qu, and P. Green, "Drivers' visual scanning behavior at signalized and unsignalized intersections: A naturalistic driving study in China," *Journal of Safety Research*, vol. 71, pp. 219–229, 2019.
- [14] A. Palazzi, D. Abati, S. Calderara, F. Solera, and R. Cucchiara, "Predicting the Driver's Focus of Attention: the DR (eye) VE Project," *IEEE Transactions on Pattern Analysis and Machine Intelligence (PAMI)*, vol. 41, no. 7, pp. 1720–1733, 2018.
- [15] A. Borji and L. Itti, "State-of-the-art in visual attention modeling," *IEEE Transactions on Pattern Analysis and Machine Intelligence (PAMI)*, vol. 35, no. 1, pp. 185–207, 2012.
- [16] A. Borji, "Saliency prediction in the deep learning era: Successes and limitations," *IEEE Transactions on Pattern Analysis and Machine Intelligence (PAMI)*, vol. 43, no. 2, pp. 679–700, 2021.
- [17] J. M. Wolfe and T. S. Horowitz, "Five factors that guide attention in visual search," *Nature Human Behaviour*, vol. 1, no. 3, p. 0058, 2017.
- [18] V. Navalpakkam and L. Itti, "Modeling the influence of task on attention," *Vision research*, vol. 45, no. 2, pp. 205–231, 2005.
- [19] S. Frintrop, *VOCUS: A visual attention system for object detection and goal-directed search*. Springer, 2006.
- [20] A. Rosenfeld, M. Biparva, and J. K. Tsotsos, "Priming neural networks," in *CVPR Workshops*, pp. 2011–2020, 2018.
- [21] V. Ramanishka, A. Das, J. Zhang, and K. Saenko, "Top-down visual saliency guided by captions," in *CVPR*, pp. 7206–7215, 2017.
- [22] Z. Ding, X. Ren, E. David, M. Vo, G. Kreiman, and M. Zhang, "Efficient zero-shot visual search via target and context-aware transformer," *arXiv:2211.13470*, 2022.
- [23] C. Cao, X. Liu, Y. Yang, Y. Yu, J. Wang, Z. Wang, Y. Huang, L. Wang, C. Huang, W. Xu, D. Ramanan, and T. S. Huang, "Look and think twice: Capturing top-down visual attention with feedback convolutional neural networks," in *ICCV*, pp. 2956–2964, 2015.
- [24] M. Biparva and J. Tsotsos, "STNet: Selective Tuning of convolutional networks for object localization," in *ICCV Workshops*, 2017.
- [25] J. Zhang, S. A. Bargal, Z. Lin, J. Brandt, X. Shen, and S. Sclaroff, "Top-down neural attention by excitation backprop," *International Journal of Computer Vision*, vol. 126, no. 10, pp. 1084–1102, 2018.
- [26] M. Ning, C. Lu, and J. Gong, "An Efficient Model for Driving Focus of Attention Prediction using Deep Learning," in *Proceedings of the IEEE International Conference on Intelligent Transportation Systems (ITSC)*, 2019.
- [27] T. Deng, H. Yan, L. Qin, T. Ngo, and B. Manjunath, "How do drivers allocate their potential attention? driving fixation prediction via convolutional neural networks," *IEEE Transactions on Intelligent Transportation Systems*, vol. 21, no. 5, pp. 2146–2154, 2019.
- [28] J. Fang, D. Yan, J. Qiao, J. Xue, and H. Yu, "DADA: Driver attention prediction in driving accident scenarios," *IEEE Transactions on Intelligent Transportation Systems*, vol. 23, no. 6, pp. 4959–4971, 2021.
- [29] D. Gopinath, G. Rosman, S. Stent, K. Terahata, L. Fletcher, B. Argall, and J. Leonard, "MAAD: A Model and Dataset for "Attended Awareness" in Driving," in *ICCV Workshops*, pp. 3426–3436, 2021.
- [30] Y. Xia, D. Zhang, J. Kim, K. Nakayama, K. Zipser, and D. Whitney, "Predicting driver attention in critical situations," in *ACCV*, 2018.
- [31] S. Gan, X. Pei, Y. Ge, Q. Wang, S. Shang, S. E. Li, and B. Nie, "Multisource adaption for driver attention prediction in arbitrary driving scenes," *IEEE Transactions on Intelligent Transportation Systems*, vol. 23, no. 11, pp. 20912–20925, 2022.
- [32] A. Pal, S. Mondal, and H. I. Christensen, "Looking at the Right Stuff" — Guided Semantic-Gaze for Autonomous Driving," in *CVPR*, 2020.
- [33] T. Deng, K. Yang, Y. Li, and H. Yan, "Where does the driver look? top-down-based saliency detection in a traffic driving environment," *IEEE Transactions on Intelligent Transportation Systems*, vol. 17, no. 7, pp. 2051–2062, 2016.
- [34] H. R. Tavakoli, E. Rahtu, J. Kannala, and A. Borji, "Digging deeper into egocentric gaze prediction," in *WACV*, 2019.
- [35] T. Deng, H. Yan, and Y.-J. Li, "Learning to boost bottom-up fixation prediction in driving environments via random forest," *IEEE Transactions on Intelligent Transportation Systems*, vol. 19, no. 9, pp. 3059–3067, 2017.
- [36] M. F. Land and D. N. Lee, "Where we look when we steer," *Nature*, vol. 369, no. 6483, pp. 742–744, 1994.
- [37] A. Borji, D. N. Sihite, and L. Itti, "Computational modeling of top-down visual attention in interactive environments," in *BMVC*, 2011.
- [38] A. Borji, D. N. Sihite, and L. Itti, "What/where to look next? Modeling top-down visual attention in complex interactive environments," *IEEE Transactions on Systems, Man, and Cybernetics: Systems*, vol. 44, no. 5, pp. 523–538, 2013.
- [39] A. Tawari and B. Kang, "A computational framework for driver's visual attention using a fully convolutional architecture," in *Proceedings of the IEEE Symposium on Intelligent Vehicles (IV)*, 2017.
- [40] P. V. Amadori, T. Fischer, and Y. Demiris, "HammerDrive: A Task-Aware Driving Visual Attention Model," *IEEE Transactions on Intelligent Transportation Systems*, vol. 23, no. 6, 2022.
- [41] S. Baee, E. Pakdamanian, I. Kim, L. Feng, V. Ordonez, and L. Barnes, "MEDIRL: Predicting the visual attention of drivers via maximum entropy deep inverse reinforcement learning," in *ICCV*, 2021.
- [42] I. Kasahara, S. Stent, and H. S. Park, "Look Both Ways: Self-supervising Driver Gaze Estimation and Road Scene Saliency," in *Proceedings of the European Conference on Computer Vision*, pp. 126–142, 2022.
- [43] J. Fang, D. Yan, J. Qiao, J. Xue, H. Wang, and S. Li, "DADA-2000: Can Driving Accident be Predicted by Driver Attention? Analyzed by A Benchmark," in *Proceedings of the IEEE Conference on Intelligent Transportation Systems (ITSC)*, 2019.
- [44] J. Ross, M. C. Morrone, M. E. Goldberg, and D. C. Burr, "Changes in visual perception at the time of saccades," *Trends in Neurosciences*, vol. 24, no. 2, pp. 113–121, 2001.

- [45] A. Vedaldi and B. Fulkerson, “VLFeat: An open and portable library of computer vision algorithms,” in *Proceedings of the ACM International Conference on Multimedia*, pp. 1469–1472, 2010.
- [46] K. Kurzahls and D. Weiskopf, “Space-time visual analytics of eye-tracking data for dynamic stimuli,” *IEEE Transactions on Visualization and Computer Graphics*, vol. 19, no. 12, pp. 2129–2138, 2013.
- [47] Z. Teed and J. Deng, “RAFT: Recurrent all-pairs field transforms for optical flow,” in *ECCV*, 2020.
- [48] P. K. Mital, T. J. Smith, R. L. Hill, and J. M. Henderson, “Clustering of gaze during dynamic scene viewing is predicted by motion,” *Cognitive computation*, vol. 3, pp. 5–24, 2011.
- [49] M. Jiang, S. Huang, J. Duan, and Q. Zhao, “Salicon: Saliency in context,” in *CVPR*, 2015.
- [50] J. Xu, M. Jiang, S. Wang, M. S. Kankanalli, and Q. Zhao, “Predicting human gaze beyond pixels,” *Journal of vision*, vol. 14, no. 1, pp. 28–28, 2014.
- [51] A. Nguyen, Z. Yan, and K. Nahrstedt, “Your attention is unique: Detecting 360-degree video saliency in head-mounted display for head movement prediction,” in *Proceedings of the ACM International Conference on Multimedia*, pp. 1190–1198, 2018.
- [52] R. Fahimi and N. D. Bruce, “On metrics for measuring scanpath similarity,” *Behavior Research Methods*, vol. 53, no. 2, pp. 609–628, 2021.
- [53] O. Lappi, P. Rinkkala, and J. Pekkanen, “Systematic observation of an expert driver’s gaze strategy – an on-road case study,” *Frontiers in psychology*, vol. 8, p. 620, 2017.
- [54] M. Kümmerer, T. S. Wallis, and M. Bethge, “DeepGaze II: Reading fixations from deep features trained on object recognition,” *arXiv:1610.01563*, 2016.
- [55] R. Droste, J. Jiao, and J. A. Noble, “Unified image and video saliency modeling,” in *ECCV*, 2020.
- [56] S. Jain, P. Yarlagadda, S. Jyoti, S. Karthik, R. Subramanian, and V. Gandhi, “ViNet: Pushing the limits of visual modality for audio-visual saliency prediction,” in *IROS*, pp. 3520–3527, 2021.
- [57] Z. Bylinskii, T. Judd, A. Oliva, A. Torralba, and F. Durand, “What do different evaluation metrics tell us about saliency models?,” *IEEE Transactions on Pattern Analysis and Machine Intelligence (PAMI)*, vol. 41, no. 3, pp. 740–757, 2018.
- [58] Z. Liu, J. Ning, Y. Cao, Y. Wei, Z. Zhang, S. Lin, and H. Hu, “Video Swin Transformer,” in *CVPR*, pp. 3202–3211, 2022.
- [59] D. Tran, L. Bourdev, R. Fergus, L. Torresani, and M. Paluri, “Learning spatiotemporal features with 3D convolutional networks,” in *ICCV*, 2015.
- [60] S. Xie, C. Sun, J. Huang, Z. Tu, and K. Murphy, “Rethinking spatiotemporal feature learning for video understanding,” in *ECCV*, pp. 318–335, 2018.
- [61] A. Vaswani, N. Shazeer, N. Parmar, J. Uszkoreit, L. Jones, A. N. Gomez, L. Kaiser, and I. Polosukhin, “Attention is all you need,” in *NeurIPS*, 2017.
- [62] A. Rasouli and I. Kotseruba, “PedFormer: Pedestrian Behavior Prediction via Cross-Modal Attention Modulation and Gated Multitask Learning,” in *ICRA*, IEEE, 2023.
- [63] J. Carreira and A. Zisserman, “Quo Vadis, Action Recognition? A New Model and the Kinetics Dataset,” in *CVPR*, 2017.
- [64] D. P. Kingma and J. Ba, “Adam: A method for stochastic optimization,” *arXiv:1412.6980*, 2014.
- [65] J. L. Campbell, C. Carney, and B. H. Kantowitz, “Human factors design guidelines for advanced traveler information systems (ATIS) and commercial vehicle operations (CVO),” Tech. Rep. FHWA-RD-98-057, US department of Transportation, Federal Highway Administration, 1998.
- [66] Z. Bylinski, “MATLAB implementation of saliency metrics,” https://github.com/cvzoya/saliency/blob/master/code_forMetrics.
- [67] R. Fahimi and N. D. Bruce, “Code for “On metrics for measuring scanpath similarity.”” <https://github.com/rAmln/saliency>.
- [68] M. Kümmerer, Z. Bylinskii, T. Judd, A. Borji, L. Itti, F. Durand, A. Oliva, and A. Torralba, “MIT/Tübingen Saliency Benchmark,” <https://saliency.tuebingen.ai/>.
- [69] M. Kümmerer, T. S. A. Wallis, and M. Bethge, “Saliency Benchmarking Made Easy: Separating Models, Maps and Metrics,” in *Proceedings of the European Conference on Computer Vision*, 2018.

A. DR(eye)VE ground truth

Here we provide additional qualitative examples to illustrate some of the shortcomings of the original ground truth in DR(eye)VE dataset. Figure 6 shows several common scenarios where fixations are incorrectly projected from the driver’s eye-tracking glasses (ETG) view to the rooftop Garmin camera view (GAR): a) when the driver looks down, the scene is not visible in the ETG view and the homography cannot be established, thus driver’s gaze is projected incorrectly onto the hood of the car; b) gaze towards the rearview mirror may be incorrectly projected onto elements of the scene behind the mirror; c) when making turns, the driver may look at the areas that are outside of the GAR camera view, however, these fixations are still mapped onto the scene in the original ground truth; d) since the GAR camera is mounted outside, the raindrops may cause issues with transformation even though the driver’s gaze is within the GAR camera field of view.

Figure 7 demonstrates the results of removing saccade to the speedometer from the ground truth. Figure 8 shows an example of ground truth containing driver’s fixations that are outside of the GAR camera field of view.

B. Task and context representation

This section details how task and context labels were used for training the proposed SCOUT model.

Table IV lists all task and context information grouped into three sets: *global context* — represents global weather, time of day, and location, *local context* — information about the upcoming intersections and actions to be taken along the route, *current action* — information about current longitudinal action (speed and acceleration) and lateral action (turns, lane changes, and driving straight).

Global context labels were provided with the dataset and are unchanged. Local context information relies on the new manual annotations and GPS data provided with the dataset. The DR(eye)VE dataset description in [14] does not specify whether the drivers knew the complete route in advance or were given step-by-step instructions. In the latter case, it is also unknown how well in advance such instructions were given and in what form. Therefore, we use guidelines designed for navigation systems that provide voice navigation commands to drivers [65]. We first compute the current distance in meters to the nearest intersection on the route using available GPS coordinates of the ego-vehicle. If that distance is larger than the max lead distance defined as $(\text{speed}(\text{km/h}) * 2.22) + 37.144$, we set it to *inf* to indicate that the intersection is too far, otherwise, we use the distance directly.

To represent current longitudinal action, we use the sequence of speed and acceleration values. Raw speed values provided with the dataset are interpolated, passed through the median filter to remove outliers, and then used to compute acceleration. For lateral action, we use manually assigned text labels since heading angle is too coarse and inaccurate



Fig. 6: Common scenarios where driver's gaze (shown as a red circle) is incorrectly projected onto the scene. Left column shows the view from the driver's eye-tracking glasses (ETG) and the right column shows the view of the rooftop Garmin camera (GAR). The following scenarios are demonstrated: a) looking down; b) checking rearview mirror; c) looking outside the GAR camera view during turns; d) raindrops on the windshield.

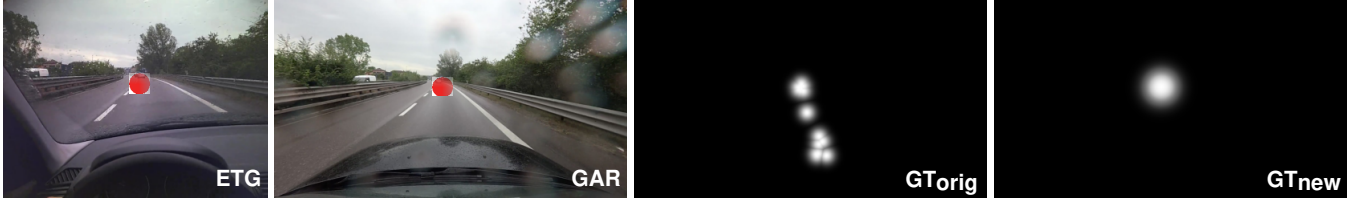


Fig. 7: Original (GT_{orig}) and new (GT_{new}) ground truth for the same frame (with fixations indicated with red circles in the drivers' (ETG) and rooftop camera (GAR) views). Note the "trail" of points in the original ground truth where the driver made a brief saccade towards the speedometer. The data points corresponding to saccaded are propagated across dozens of frames due to the aggregation procedure. These are absent in the new ground truth shown in the leftmost image.



Fig. 8: Original (GT_{orig}) and new (GT_{new}) ground truth for the same frame (with fixations indicated with the red circle in the drivers' (ETG) view). The driver is looking through the side window, however, in the original ground truth, points representing saccades in the past frames and out-of-bounds fixations are still projected onto the scene in a random pattern. In the new ground truth, to preserve some gaze information, we push out-of-bounds fixations towards the edge of the frame to indicate the approximate direction of where the driver is attending.

and yaw information is not available. If there is more than one label in the sample, the most frequently occurring label is chosen.

C. Benchmark results

1) *Implementation of Kullback-Leibler divergence:* Kullback-Leibler divergence (KLD) is the key dissimilarity metric commonly reported when evaluating saliency algorithms [57].

KLD is defined as $P||Q = \sum p_i \ln \frac{p_i}{q_i}$, where P and

Q are two distributions being compared. Since saliency maps are usually sparse, cases when non-zero value in one image ($p_i > 0$) corresponds to zero value in another ($q_i = 0$) occur frequently. To prevent division by zero, a small constant ϵ is added to the denominator in the equation above. Consequently, if the saliency values are small, the result can be dominated by this parameter. Depending on the implementation, ϵ may be set differently. Below are three typical values used:

- MATLAB machine epsilon: $\epsilon = 1.1920929e - 07$;

TABLE IV: Task and context representation

Category	Features	Values
Global context	Weather	text label: sunny, cloudy, or rainy
	Time of day	text label: morning, evening, night
Local context	Location	text label: highway, urban, suburban
	Distance to intersection (m)	numeric value
	Priority	right-of-way, yield
Current action	Next action	text label: turn right, turn left, drive straight
	Speed (km/h)	numeric array
	Acceleration (m/s ²)	numeric array
	Action	text label: turn right/left, lane change right/left, drive straight

- numpy machine epsilon: $\epsilon = 2.2204e - 16^3$ (default in Python implementations);
- A small constant: $\epsilon = 0.0001$.

The Python implementation of KLD used in the DR(eye)VE evaluation code⁴ follows the widely used Matlab implementation [66] for the MIT saliency benchmark⁵, but this Python version is numerically unstable for some inputs. We compared the DR(eye)VE version of KLD to two other Python implementations: Fahimi & Bruce [52], [67] and pysaliency [68], [69], the official evaluation code for the MIT/Tuebingen saliency benchmark⁶.

Table V shows results of testing different implementations with different values of ϵ on three test cases:

- 1) *Two identical randomly generated images.* KLD for two identical images is expected to be 0, however, DR(eye)VE implementation fails to produce this value with MATLAB and small constant ϵ for two randomly generated identical images (1000×1000 px).
- 2) *Two different randomly generated images.* Similarly, DR(eye)VE implementation of KLD diverges significantly for MATLAB and small constant ϵ when tested on two *different* randomly generated images. Two other implementations remain stable with small differences in the sixth decimal.
- 3) *Randomly selected ground truth and predicted saliency maps from DR(eye)VE.* DR(eye)VE implementation diverges from others on a pair of ground truth and predicted saliency maps randomly selected from the

³`np.finfo(np.float32).eps`

⁴<https://github.com/ndrplz/dreyeve/blob/master/experiments/metrics/metrics.py>

⁵saliency.mit.edu

⁶saliency.tuebingen.ai

dataset. Here, even using the default ϵ generates results different from other implementations.

Table VI shows the evaluation results of BDD-ANet [30], DReyeVENet [14], and ADA [31], using DR(eye)VE implementation with MATLAB ϵ and Fahimi & Bruce code with Numpy ϵ . The results obtained with the DR(eye)VE implementation with MATLAB ϵ replicate the KLD values reported in the literature. Fahimi & Bruce implementation produces different absolute values, but preserves the relative ranking of the models. Since finding the cause of the numerical issues is beyond the scope of these experiments, we

TABLE V: Results of testing different KLD implementations with several standard values of ϵ on three scenarios. Diverging results of DR(eye)VE implementation are highlighted in orange.

Data	Implementation	ϵ		
		MATLAB 1.19E-07	Numpy 2.22E-16	Small constant 0.0001
Identical images	DR(eye)VE	-0.029013	0	-2.771208
	Fahimi & Bruce	0	0	0
	pysaliency	0	0	0
Random images	DR(eye)VE	0.087539	0.499305	-5.205599
	Fahimi & Bruce	0.499304	0.499305	0.498398
	pysaliency	0.499304	0.499306	0.498398
Salmaps from DR(eye)VE	DR(eye)VE	2.322985	7.277252	-2.70738
	Fahimi & Bruce	5.135229	9.888739	3.525612
	pysaliency	5.135229	9.888739	3.525612

TABLE VI: Evaluation results on the original DR(eye)VE dataset ground truth using DR(eye)VE implementation with MATLAB ϵ and Fahimi & Bruce code with Numpy ϵ .

Model	KLD (DR(eye)VE implementation)	KLD (Fahimi & Bruce)
BDD-ANet	1.92	3.15
DReyeVENet	1.59	2.63
ADA	1.56	2.33

report the results for all algorithms using the more accurate Fahimi & Bruce implementation with Python ϵ .

2) *Additional benchmark results:* Table VII shows additional evaluation results on action and context sequences and CC, SIM, and NSS metrics.

D. Additional SCOUT results

Table VIII reports additional evaluation results on action and context sequences and CC, SIM, and NSS metrics for variants of the proposed SCOUT model.

TABLE VII: Additional benchmark results on CC, NSS, and SIM metrics. \uparrow indicates that larger values are better.

		Actions (CC↑)					Context (CC↑)							
Model		Stop	None	Lat	Lon	Lat+Lon	Roundabout		Highway ramp		Signalized		Unsignalized	
		RoW	Yield	RoW	Yield	RoW	Yield	RoW	Yield	RoW	Yield	RoW	Yield	
Image	CDNN†	0.13	0.54	0.31	0.33	0.18	0.18	0.07	0.66	0.24	0.30	0.32	0.37	0.06
	CDNN**	0.27	0.75	0.50	0.61	0.38	0.57	0.19	0.77	0.50	0.57	0.40	0.66	0.21
	DeepGaze II	0.19	0.33	0.23	0.28	0.16	0.13	0.08	0.35	0.23	0.23	0.18	0.26	0.06
	UNISAL	0.33	0.44	0.31	0.38	0.22	0.22	0.17	0.45	0.30	0.33	0.30	0.34	0.08
Video	UNISAL	0.32	0.59	0.42	0.52	0.29	0.36	0.22	0.64	0.38	0.50	0.42	0.52	0.14
	ViNet	0.34	0.65	0.46	0.55	0.32	0.37	0.21	0.68	0.48	0.51	0.44	0.57	0.16
	ViNet*	0.32	0.74	0.51	0.61	0.40	0.43	0.25	0.75	0.51	0.58	0.38	0.64	0.30
	DreyeVENet**	0.34	0.75	0.50	0.61	0.41	0.52	0.18	0.78	0.46	0.62	0.47	0.65	0.23
	BDD-A-Net†	0.34	0.65	0.40	0.52	0.26	0.35	0.21	0.70	0.36	0.48	0.33	0.52	0.11
	BDD-A-Net**	0.31	0.72	0.46	0.59	0.35	0.37	0.23	0.75	0.44	0.53	0.42	0.61	0.20
	ADA	0.39	0.75	0.49	0.63	0.35	0.52	0.26	0.77	0.48	0.59	0.45	0.63	0.19

		Actions (NSS↑)					Context (NSS↑)							
Model		Stop	None	Lat	Lon	Lat+Lon	Roundabout		Highway ramp		Signalized		Unsignalized	
		RoW	Yield	RoW	Yield	RoW	Yield	RoW	Yield	RoW	Yield	RoW	Yield	
Image	CDNN†	0.55	1.77	1.10	1.24	0.71	0.75	0.26	2.16	0.88	1.16	1.21	1.28	0.20
	CDNN**	1.14	2.20	1.56	1.95	1.23	1.74	0.67	2.27	1.43	1.77	1.36	1.97	0.76
	DeepGaze II	0.78	1.23	0.91	1.12	0.69	0.58	0.42	1.24	0.87	0.82	0.82	1.03	0.25
	UNISAL	1.43	1.87	1.31	1.64	0.94	1.01	0.71	1.92	1.22	1.36	1.33	1.51	0.31
Video	UNISAL	1.34	2.23	1.51	1.94	1.07	1.50	0.79	2.38	1.48	1.80	1.54	1.93	0.50
	ViNet	1.43	2.40	1.67	2.09	1.21	1.48	0.77	2.54	1.66	1.93	1.66	2.10	0.55
	ViNet*	1.27	2.13	1.56	1.93	1.31	1.50	0.86	2.17	1.45	1.83	1.34	1.94	1.03
	DreyeVENet**	1.38	2.15	1.54	1.90	1.33	1.71	0.64	2.21	1.37	1.86	1.53	1.96	0.85
	BDD-A-Net†	1.36	1.86	1.26	1.67	0.86	1.25	0.71	1.94	1.06	1.53	1.14	1.61	0.34
	BDD-A-Net**	1.32	2.22	1.49	1.97	1.20	1.39	0.78	2.31	1.38	1.74	1.46	1.98	0.68
	ADA	1.57	2.11	1.50	1.95	1.14	1.83	0.89	2.16	1.35	1.81	1.59	1.86	0.62

		Actions (SIM↑)					Context (SIM↑)							
Model		Stop	None	Lat	Lon	Lat+Lon	Roundabout		Highway ramp		Signalized		Unsignalized	
		RoW	Yield	RoW	Yield	RoW	Yield	RoW	Yield	RoW	Yield	RoW	Yield	
Image	CDNN†	0.12	0.38	0.25	0.25	0.16	0.16	0.10	0.46	0.22	0.22	0.23	0.27	0.08
	CDNN**	0.23	0.61	0.41	0.48	0.31	0.42	0.19	0.63	0.41	0.42	0.31	0.51	0.18
	DeepGaze II	0.13	0.17	0.15	0.16	0.12	0.11	0.11	0.17	0.13	0.13	0.12	0.14	0.08
	UNISAL	0.19	0.22	0.18	0.20	0.15	0.16	0.14	0.22	0.16	0.18	0.17	0.18	0.09
Video	UNISAL	0.26	0.42	0.32	0.38	0.24	0.28	0.19	0.45	0.29	0.36	0.30	0.37	0.14
	ViNet	0.25	0.43	0.32	0.37	0.24	0.26	0.19	0.45	0.34	0.34	0.29	0.37	0.14
	ViNet*	0.24	0.53	0.37	0.44	0.29	0.31	0.20	0.53	0.37	0.41	0.27	0.45	0.20
	DreyeVENet**	0.27	0.62	0.42	0.50	0.34	0.43	0.17	0.65	0.38	0.50	0.38	0.54	0.19
	BDD-A-Net†	0.24	0.46	0.30	0.38	0.22	0.26	0.18	0.51	0.29	0.32	0.24	0.35	0.12
	BDD-A-Net**	0.23	0.54	0.36	0.43	0.27	0.27	0.20	0.57	0.36	0.37	0.30	0.44	0.16
	ADA	0.28	0.57	0.38	0.47	0.28	0.30	0.21	0.57	0.39	0.41	0.32	0.46	0.16

* — model is trained on the data; † — model for drivers' gaze prediction. Notation: Stop — vehicle is stopped, Lat — lateral actions only, Lon — longitudinal only, None — no action, RoW — ego-vehicle has right-of-way. Green and red colors indicate the best and worst values.

TABLE VIII: Additional results for variants of SCOUT model on CC, NSS, and SIM metrics. \uparrow indicates that larger values are better. Best and second-best values are shown as **bold** and underlined.

		Actions (CC \uparrow)					Context (CC \uparrow)							
Model		Stop	None	Lat	Lon	Lat+Lon	Roundabout		Highway ramp		Signalized		Unsignalized	
							RoW	Yield	RoW	Yield	RoW	Yield	RoW	Yield
ADA		0.39	0.75	0.49	0.63	0.35	<u>0.52</u>	0.26	0.77	0.48	0.59	<u>0.45</u>	0.63	0.19
ViNet		0.32	<u>0.74</u>	<u>0.51</u>	0.61	0.40	0.43	0.25	<u>0.75</u>	0.51	0.58	0.38	0.64	0.30
SCOUT	w/o task	0.27	0.70	0.50	0.57	0.38	0.53	0.16	0.72	0.48	0.59	0.25	0.61	0.17
	w/o task + weighted loss	0.35	0.72	0.50	0.61	0.42	0.47	0.22	0.73	0.45	0.62	0.40	0.64	0.24
	w/o task + weighted sampling	<u>0.30</u>	0.72	0.50	0.60	0.42	<u>0.45</u>	0.21	<u>0.75</u>	0.46	0.60	0.41	0.64	0.25
	w/ task CA[3]	0.34	0.73	0.50	<u>0.62</u>	0.43	0.41	<u>0.32</u>	<u>0.75</u>	0.46	0.61	0.44	0.63	<u>0.33</u>
	w/ task GC+LC+CA [2, 3, 4]	0.37	0.73	0.53	<u>0.62</u>	0.46	0.38	0.30	<u>0.75</u>	0.46	<u>0.63</u>	0.25	<u>0.66</u>	<u>0.33</u>
	w/ task GC+LC+CA [3]	0.31	0.73	<u>0.51</u>	0.61	0.43	0.46	0.26	<u>0.75</u>	0.46	0.62	0.39	0.63	0.28
w/ task LC [2]		0.34	<u>0.74</u>	0.53	<u>0.62</u>	0.50	0.42	0.34	<u>0.75</u>	<u>0.49</u>	0.64	0.46	0.67	0.34
		Actions (NSS \uparrow)					Context (NSS \uparrow)							
Model		Stop	None	Lat	Lon	Lat+Lon	Roundabout		Highway ramp		Signalized		Unsignalized	
							RoW	Yield	RoW	Yield	RoW	Yield	RoW	Yield
ADA		1.57	2.11	1.50	1.95	1.14	1.83	0.89	2.16	1.35	1.81	1.59	1.86	0.62
ViNet		1.27	2.13	1.56	1.93	1.31	1.50	0.86	2.17	1.45	1.83	1.34	1.94	1.03
SCOUT	w/o task	1.63	4.40	2.97	3.51	2.20	3.07	0.92	4.53	<u>2.97</u>	3.55	1.54	3.76	0.98
	w/o task + weighted loss	2.07	4.51	3.03	3.70	2.48	2.70	1.17	4.58	2.77	3.72	2.47	3.91	1.46
	w/o task + weighted sampling	1.80	4.52	3.00	3.68	2.50	<u>2.59</u>	1.17	4.73	2.77	3.57	2.57	3.91	1.65
	w/ task CA[3]	2.07	<u>4.57</u>	3.05	3.77	2.59	2.39	<u>1.99</u>	4.70	2.81	3.68	<u>2.76</u>	3.90	<u>2.34</u>
	w/ task GC+LC+CA [2, 3, 4]	2.23	4.56	<u>3.21</u>	<u>3.79</u>	<u>2.77</u>	2.18	1.88	4.70	2.78	<u>3.77</u>	1.59	<u>4.02</u>	<u>2.34</u>
	w/ task GC+LC+CA [3]	1.87	4.53	3.04	3.72	2.52	2.65	1.49	4.72	2.80	3.68	2.40	3.86	1.81
w/ task LC [2]		<u>2.03</u>	4.64	3.24	3.82	3.09	2.40	2.09	<u>4.71</u>	3.00	3.80	2.91	4.12	2.43
		Actions (SIM \uparrow)					Context (SIM \uparrow)							
Model		Stop	None	Lat	Lon	Lat+Lon	Roundabout		Highway ramp		Signalized		Unsignalized	
							RoW	Yield	RoW	Yield	RoW	Yield	RoW	Yield
ADA		<u>0.28</u>	0.57	0.38	0.47	0.28	0.30	0.21	0.57	<u>0.39</u>	0.41	<u>0.32</u>	0.46	0.16
ViNet		0.24	0.53	0.37	0.44	0.29	0.31	0.20	0.53	0.37	0.41	0.27	0.45	0.20
SCOUT	w/o task	0.23	0.58	0.41	0.47	0.31	0.41	0.16	0.59	0.41	0.47	0.23	0.50	0.16
	w/o task + weighted loss	0.26	0.57	0.40	0.48	0.33	<u>0.36</u>	0.20	0.57	0.36	0.48	0.29	0.49	0.18
	w/o task + weighted sampling	0.24	0.58	0.41	0.48	0.34	<u>0.36</u>	0.19	0.60	0.37	0.47	<u>0.32</u>	<u>0.51</u>	0.20
	w/ task CA[3]	0.27	<u>0.60</u>	0.41	<u>0.49</u>	0.34	0.33	<u>0.25</u>	0.61	0.38	<u>0.49</u>	0.33	<u>0.51</u>	<u>0.22</u>
	w/ task GC+LC+CA [2, 3, 4]	0.30	<u>0.60</u>	<u>0.42</u>	<u>0.49</u>	<u>0.35</u>	0.30	<u>0.25</u>	0.61	0.38	0.48	0.21	<u>0.51</u>	0.23
	w/ task GC+LC+CA [3]	0.23	0.57	0.40	0.48	0.33	0.34	0.22	0.61	0.37	0.47	0.26	0.49	0.19
w/ task LC [2]		0.26	0.61	0.43	0.50	0.38	0.33	0.26	0.61	<u>0.39</u>	0.51	<u>0.32</u>	0.54	<u>0.22</u>

* — model is trained on the data; \dagger — model for drivers' gaze prediction. Notation: Stop — vehicle is stopped, Lat — lateral actions only, Lon — longitudinal only, None — no action, RoW — ego-vehicle has right-of-way.